Materials Science & Engineering A 835 (2022) 142654

Contents lists available at ScienceDirect

Materials Science & Engineering A

journal homepage: www.elsevier.com/locate/msea

In-situ tensile and fatigue behavior of electrical grade Cu alloy for subsea cables

Di Wan [a,*], Anette Brocks Hagen [b], Luigi Mario Viespoli [b], Audun Johanson [c], Filippo Berto [a], Antonio Alvaro [a,b]

[a] Department of Mechanical and Industrial Engineering, Norwegian University of Science and Technology, Richard Birkelands vei 2B, 7491, Trondheim, Norway
[b] Department of Materials and Nanotechnology, SINTEF Industry, 7456, Trondheim, Norway
[c] Nexans Norway, Innspurten 9, 0663, Oslo, Norway

ARTICLE INFO

Keywords:
Copper
Tensile test
Cyclic loading
Scanning electron microscopy (SEM)
Electron backscattered diffraction (EBSD)
Electron channeling contrast imaging (ECCI)

ABSTRACT

Distribution of electrical energy through subsea power cables has an increasingly important role in the renewable power generation. The majority of the subsea cables uses copper (Cu) as a conductor material. Cables suspended from sea level to sea floor are subjected to both static and cyclic loads that can introduce microstructural damage due to fatigue, creep and their interaction. In addition, since the manufacturing process of the stranded conductor results in Cu-materials with superficial irregularities and metallurgical anisotropy, the material performances need to be carefully addressed in order to reliably assess the wires life. In order to provide a deeper insight into the occurring damage mechanisms, monotonic and cyclic tests of micro-sized Cu tensile specimens were carried out using *in-situ* micromechanical testing, inside a scanning electron microscopy (SEM) equipped with an electron backscatter diffraction. Tensile and cyclic loading behavior are discussed in correlation with the damage mechanisms observed directly and post-mortem. The twin boundary fraction in the microstructure is found to be linked to the deformation status, and thus can potentially be used as an indicator for predicting the remaining life of the material under service conditions.

1. Introduction

At the present day, a vast network of subsea cables is installed for high voltage power transfer, across stretches of water, often several hundreds of kilometers long, to neighboring landmasses and islands, effectively interconnecting different national grids to balance energy supply and demand. In the recent years, floating wind farms have become an important solution with respect to renewable energy. This includes dynamic power cables, hanging from/connected to the floating units, that will be subjected to fatigue loading from waves, current and motion from the floating structure [1]. Therefore, the structural integrity of the conductor must be carefully evaluated, through estimation of load history, material response and degradation during the operational life.

Electrolytic Tough Pitch (ETP) copper is a high purity copper (>99.9 wt%) frequently used for the transmission of electrical energy due to a low resistivity (Copper Development Association Inc.). The ductile damage and failures of pure copper have been object of different studies [2,3], as well as the impact of strain rate and temperature [4]. The material can in fact be subjected to creep deformation even at temperatures at and slightly above room temperature, if the stress level is sufficiently high to activate relevant mechanisms [5]. Creep deformation has a detrimental impact not only on the ultimate load, but also on the ability to withstand fatigue loading [6–8], which is of paramount importance for the reliability of floating systems [9,10].

The conductor in a dynamic power cable application is subjected to a complex loading system, with several factors interacting and potentially causing the failure of the infrastructure. In particular, since the operational temperature at the core generally ranges between room temperature and 90 °C, the positive mean stress inherent by the cable weight and local residual stresses, leads to the activation to creep phenomena which interact with the fatigue damage. In this sense, the impact of loading frequency/strain rate on the material integrity is an important factor which has to be included in the life assessment of the alloy used. The contact between the wires composing the conductor might also cause a fatigue life reduction due to the detrimental effect of fretting

* Corresponding author.
E-mail address: di.wan@ntnu.no (D. Wan).

https://doi.org/10.1016/j.msea.2022.142654
Received 16 August 2021; Received in revised form 14 December 2021; Accepted 7 January 2022
Available online 11 January 2022

fatigue.

As a typical face-centered cubic (FCC) crystal, copper has been used as model materials for studying various deformation and fracture mechanisms of FCC materials [11–14]. Moreover, the fatigue or cyclic loading response of copper attracts researchers' attention to a large extent [15–18]. At a microscale, the deformation structure – boundary interaction is of great interest as the boundaries can work as active barriers for dislocation slip and thus strengthening the material. When it comes to copper, the twin boundaries, especially the coherent twin boundaries, are appreciated due to the strengthening effect to the material's mechanical performance without significantly increasing the electrical resistivity due to their coherent characteristics to the matrix [19]. Yet, most of the studies on the twin boundaries in copper are focusing on the nanotwin in nanocrystalline/ultra-fine grained copper samples (e.g. Refs. [19–21]), and due to the intrinsic size effect [22], the resulting conclusions from the nano-scale studies may not be directly applicable to macro-scale applications. Llanes et al. [23–25] did systematic studies on the cyclic deformation of polycrystalline copper, focusing on the persistent slip bands (PSBs) adjacent to the twins, and confirmed the same phenomenon observed by other researchers [26, 27]. However, the cracking behavior in the presence of a twin boundary has its complexities from stacking fault energy, slip mode, and the dislocation – twin interaction both in the matrix and in the twin region [28,29]. As a result, the understanding on the dislocation – twin interaction during cyclic loading is still limited.

In the present work, the influence of monotonic and cyclic loading on the damage mechanism of ETP copper extruded wires, are investigated. Tensile tests were performed in the extrusion direction at three different strain rates while continuously observing the specimen surface evolution with a scanning electron microscope (SEM). Electron backscatter diffraction (EBSD) analysis was performed before and after tensile testing, along with SEM fractography. The cyclic tests were performed at different load ratios R and stress amplitudes to observe the damage evolution on the surface of the specimen as a function of the applied mean stress. A few of the tests were continued until failure occurred. The SEM observation of the surface evolution, the EBSD analysis and electron channeling contrast imaging (ECCI) performed, with a focus on the twin boundary evolution, allowed for valuable insight of the real-time deformation behavior and mechanical response with respect to the applied loads.

2. Material and experimental

2.1. Material

The material used in this study is a cold-drawn and annealed ETP Cu alloy with a purity of >99.90 wt% Cu. The as-received Cu is a trapezoidal shaped wire with a cross section of ~5 × 6 mm^2. Dog-bone shaped tensile specimens were manufactured with the dimensions shown in Fig. 1a. The microstructure was investigated prior to testing with electron backscatter analysis (EBSD) analysis using a Quanta 650 FEG scanning electron microscope (SEM, ThermoFisher Inc., USA) with an acceleration voltage of 20 kV and a working distance of 15 mm, and the incident beam has a 70° angle with respect to the sample surface. NORDIF software was used to collect the diffraction pattern, and the patterns were off-line indexed by the OIM Data Collection software. The orientation map from EBSD analysis of the undeformed material is shown in Fig. 1b. Tensile specimens were mechanically ground and polished step by step down to 1 μm diamond paste and electropolished at 20 V for 10 s in D2 electrolyte, before EBSD analysis and testing.

2.2. Tensile tests

The tensile tests were conducted in the SEM while continuously recording the top surface deformation as a series of digital still images. A 5 kN tensile/compression module (Kammrath & Weiss GmbH, Germany) was used for testing and controlled directly from a computer with DDS32 software. The specimens were gripped with clamps that moves simultaneously for both ends. Thus, the center of the specimen is standing still enabling high-quality video recording. Monotonic loading was performed with three different displacement rates: 0.2, 2 and 20 μm/s, which correspond to nominal strain rates of 1 × 10^{-4}, 1 × 10^{-3} and 1 × 10^{-2} s^{-1}, respectively, calculated considering the reducing section of the specimens. It should be noted that the reduced region of the specimen is not uniform in geometry, and therefore the strain rates as well as the local strain level can be nonuniform. For the analysis regions of interest (ROIs), the local strain level has been additionally correlated by the real-time SEM images.

2.3. Cyclic tests

The influence of stress amplitude (σ_a, defined as half of the difference between the maximum and minimum stresses during a loading cycle) and mean stress (σ_m, defined as the mean value of the maximum and minimum stresses during a loading cycle) on the micromechanical deformation behavior was investigated using the tensile/compression module in a load-controlled mode (i.e., stress-controlled mode) using a fixed displacement rate of 20 μm/s. This corresponds to an initial nominal strain rate of 1 × 10^{-2} s^{-1}. In the beginning, a fully reversed tensile-compression cyclic loading was conducted on the specimen R0 with a stress range from −80 MPa to 80 MPa ($\sigma_m = 0$ and $\sigma_a = 80$ MPa). The test was interrupted after 2000 cycles, and post characterization was performed to understand the basic cyclic deformation behavior in the microstructure evolution. Tests with different mean stresses and stress

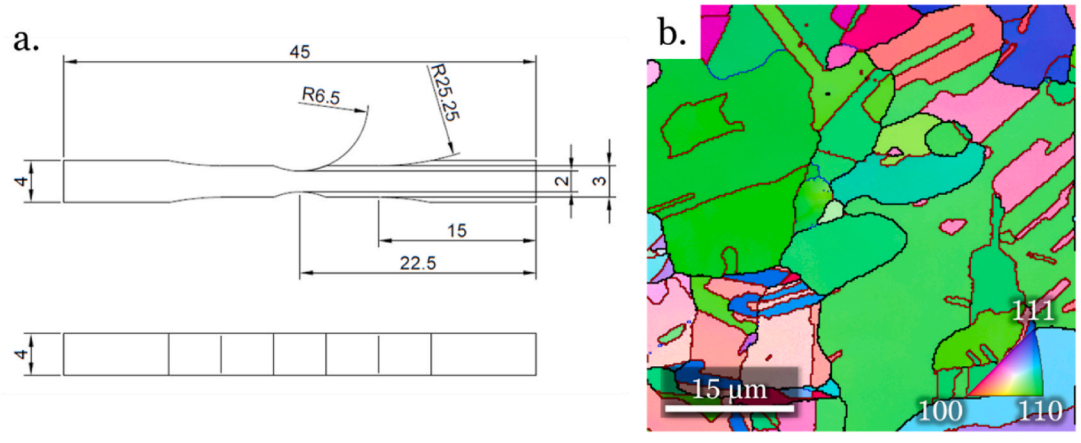

Fig. 1. a. Specimen dimension for tensile -and cyclic testing (units in mm) and b. The initial microstructure shown as extrusion direction – orientation map by EBSD.

amplitudes were subsequently performed. The specimen R1 ($\sigma_m = 200$ MPa and $\sigma_a = 50$ MPa) failed after 34 cycles due to the high load level (mainly due to the maximum stress during the cyclic loading). Therefore, a reduced stress amplitude ($\sigma_a = 25$ MPa) was chosen for the specimen R2 with the same mean stress level ($\sigma_m = 200$ MPa), and the specimen failed after 2624 cycles. The following tests on the R3 ($\sigma_m = 200$ MPa and $\sigma_a = 25$ MPa), R4 ($\sigma_m = 150$ MPa and $\sigma_a = 50$ MPa) and R5 ($\sigma_m = 150$ MPa and $\sigma_a = 25$ MPa) specimens were interrupted at a same number of cycles (1150) for microstructural characterization and analysis. The stress amplitudes and mean stresses used in the tests are given in Table 1.

2.4. Fractography and post analysis

Fractography was performed on all specimens after tensile and cyclic testing. In addition, fractured tensile specimens were prepared again by grinding, mechanical polishing and electrolytic polishing, in order to remove the surface topography. The fractured specimens were successively characterized by EBSD with the same parameters described in Section 2.1. For each specimen, 50 × 50 μm^2 scanning areas were repeated at least four times in random representative regions in order to obtain a higher statistical reliability of the measurements. The microstructure of the fractured specimens was evaluated by using the IPF-orientation maps, grain boundaries (GBs) maps overlapped with image quality (IQ) value, kernel average misorientation (KAM) maps, grain orientation spread (GOS) maps and finally texture characterization. To investigate the dislocation structures of the deformed specimens, electron channeling contrast imaging (ECCI) was conducted in the SEM with an accelerating voltage of 30 kV at a working distance of ~6 mm. The specimens were slight tilted (less than 3°) in order to meet the two-beam diffraction condition and thus obtain the optimum contrast for an optimal characterization of the deformation structures [30]. This technique has been widely used in dislocation structure analysis [31,32] and/or twin analysis [33,34].

3. Results

3.1. Tensile properties

Fig. 2a summarizes the engineering stress-strain curves for the Cu specimens at the different nominal strain rates of 1×10^{-4}, 1×10^{-3} and 1×10^{-2} s^{-1}. The yield strength and ultimate tensile strength values are presented in Table 2. The stress-strain characteristics revealed a uniform strain up to the ultimate tensile stress, followed by a drastic load drop due to deformation localization (necking) and the final rupture. Overall, the mechanical response shows a ductile behavior, typically obtained for this material [35]. Fig. 2b shows the work hardening rate (WHR, defined as $\Theta = d\sigma_t/d\varepsilon_t$) as a function of true strain (calculated from the conventional constant volume approach) for all three strain rates. For all tests, the WHR steeply decreases in the elastic-plastic transition stage until a true strain of ~ 0.2 is reached. After such pronounced decline, the WHR increases slightly with the increase in the true strain and reaches a constant value up to ~0.55. The slowest test (1×10^{-4} s^{-1}) shows a relatively lower WHR in comparison with that of the faster tests (1×10^{-3} s^{-1} and 1×10^{-2} s^{-1}).

Table 1
Cyclic test conditions and cycles to failure.

Specimen	Mean stress σ_m [MPa]	Stress amplitude σ_a [MPa]	Cycles, N [cycle]	Stress range [MPa]	Comment
R0	0	80	2000	−80–80	Interrupted
R1	200	50	34	150–250	Failure
R2		25	2624	175–225	Failure
R3		25	1150	175–225	Interrupted
R4	150	50	1150	100–200	Interrupted
R5		25	1150	125–175	Interrupted

3.2. Tensile deformation morphologies

Fig. 3 shows the fracture surface from the specimens tested at the highest and lowest strain rate, i.e., 1×10^{-2} and 1×10^{-4} s^{-1}, respectively. As shown in Fig. 3, surface investigations revealed a similar ductile fracture morphology for both cases. The final cross-section area is measured to 1.703 mm^2 and 1.723 mm^2 for the specimens tested at 1×10^{-2} s^{-1} and 1×10^{-4} s^{-1}, respectively, an increase of about 1.2%. No significant differences in the fracture behavior are found between these two specimens.

Fig. 4 shows the EBSD orientation map, IQ map with grain boundary distribution, the KAM and the GOS map of the deformed microstructure at the top surface of the fracture tensile specimen. The microstructure is composed of multiple sub grains and dispersion of grain orientations after severe plastic deformation (Fig. 4a). As shown in the IQ map with GB distribution (Fig. 4b), the microstructure contains a dense network of GBs after sub-grain formation, with 62.6% of them being low-angle boundaries (LAGBs), 34.7% high-angle grain boundary (HAGB) and 7.1% being Σ3 twin boundaries (TBs). The LAGB is defined as a boundary with 2–15° misorientation, whereas HAGB is that with a misorientation >15°. The coincidence site lattice (CSL) boundary Σ3 is considered as TBs in this work since it shares the same character with the annealing TBs where a <111>−60° relationship can be noted.

The KAM data represents the average misorientation angle of a given point with respect to its neighbors and describes the local dislocation density distribution. Fig. 4c displays the KAM (0–5°) map and reveals the tendency for the local deformation to polygonize into sub-grains. The GOS analysis was also used to map the deformation behavior in terms of internal rotations of micro volumes such as grains or sub-grains within the grains. As shown in Fig. 4d, highly deformed regions, consisting of multiple sub-grains, obtain high GOS values (up to 10°), i.e., the red areas. Unlike KAM that detects plasticity induced deformation in local sites, GOS displays the total misorientation in a grain and color the grains accordingly.

Fig. 5 shows the normal direction orientation maps obtained from EBSD analysis of undeformed, ~5% strain, and close to fracture Cu, respectively. The recorded fractions of each type of grain boundary are presented in Table 3. The results reveal a decreasing fraction of Σ3 boundaries with increasing tensile deformation, with ~60% in the undeformed condition and ~7% after final fracture.

3.3. Cyclic loading data

Fig. 6 shows the mechanical response under cyclic loading of sample R0 ($\sigma_a = 80$ MPa and $\sigma_m = 0$). The apparent discontinuity of the hysteresis cycles (Fig. 6a, quadrant: Strain 0–0.5%/Stress 0–10 MPa) is due to a certain degree of relaxation in the geared actuation system, which comes into play in the transition from positive to negative stress. A cyclic softening behavior is recorded based on the analysis in Fig. 6b, where an increasing strain amplitude is noted with respect to the number of cycles, while the stress level is set constant.

Fig. 7 shows the cyclic response from the tests of R3, R4 and R5 specimens in terms of accumulated strain level (ratchetting strain) versus number of cycles. Clearly, the accumulated strain increases with the number of cycles, i.e. the specimen is softened during cyclic loading for all the three cases. In R3, the strain rate first decreases, then increases slightly after approx. 1000 cycles. On the other hand, for R4 and R5, the strain rate per cycle decreases in the beginning but stabilizes to a constant level until the test is terminated. It must be pointed out that the small disturbances in the curves arose from the interruption of the tests when the *in-situ* SEM images were taken.

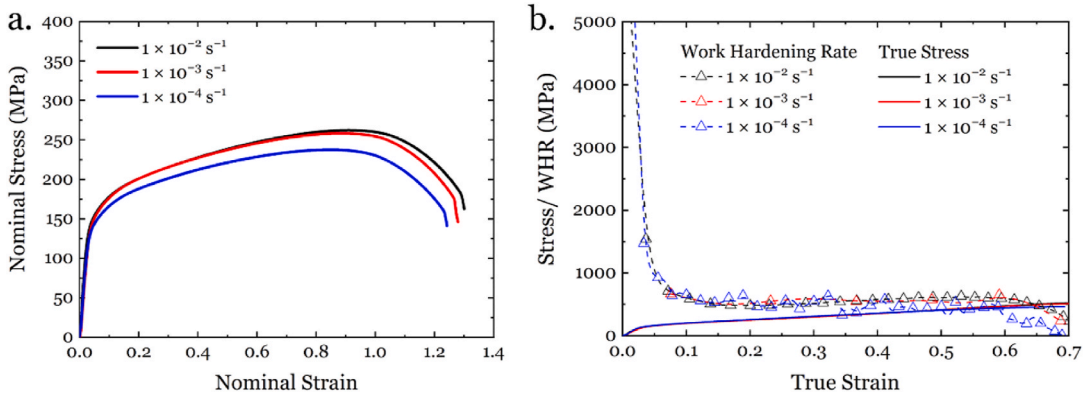

Fig. 2. a. Engineering stress-strain curves and b. True stress-strain curves (solid lines) with work hardening rate (WHR, dashed lines with symbols) from monotonic tensile tests at initial strain rates of 1×10^{-2}, 1×10^{-3} and 1×10^{-4} s^{-1}.

Table 2
Mechanical properties of the tested Cu specimens.

Nominal strain rate [s^{-1}]	Yielding strength [MPa]	Ultimate tensile strength [MPa]
1×10^{-2}	155	262
1×10^{-3}	152	258
1×10^{-4}	145	235

3.4. Cyclic deformation behavior

Fig. 8 shows the SEM images of the *in-situ* cyclically loaded specimen R0 ($\sigma_m = 0$ and $\sigma_a = 80$ MPa). After 2000 cycles, the specimen surface still shows flat surface at a lower magnification (Fig. 8a), but a deeper analysis at a higher magnification (Fig. 8b) revealed the appearance of damage at grain boundaries (Fig. 8c) and grain triple junctions (Fig. 8d). Fig. 9 shows the ECCI analysis in this specimen. The GB damage in Fig. 8c is further analyzed in Fig. 9a. Observation revealed GB decohesion from the particles with white contrast, which were further confirmed to be oxides by means of energy dispersive X-ray spectroscopy (EDS). The deformation structure in the grain matrix is mostly arranged in the form of dislocation cells. It is also interesting to observe that the interaction of such dislocation walls with the existing annealing TBs, generate steps on the TBs (Fig. 9b). It can be inferred that the dislocation arrangements are "consuming" the annealing twins during cyclic loading.

Fig. 10 shows EBSD and ECCI analysis of deformed microstructure after cyclic testing of specimen R3, R4 and R5. Overall, the cyclic loading introduced dislocation wall and cell structures with increasing stresses (both in σ_m and σ_a), the fraction of annealing TBs decreases. In R3, about 17.2% TBs are detected from the EBSD analysis, while 56% for R4 and 61.1% for R5. The deformation structure in these specimens is revealed as dislocation walls, cells and subgrains as can be seen from both the KAM maps and ECCI analysis in Fig. 10a_2 to c_2 and a_3 to c_3. The R3 specimen has a significant distorted grain shape in elongated form along tensile direction, meaning the global strain level is much higher; the R4 and R5 specimens still keep the equiaxed grain shape. This is in agreement with the ratchetting strain level recorded in Fig. 7. Deeper analysis of R5 shows mainly the presence of dislocation walls that did not fully form a stable polygonized cell structure (Fig. 10a_3 to c_3). When the σ_m and σ_a increase, the deformation becomes more severe such that dislocation cells start to form and coexist with the dislocation walls in R4 (Fig. 10a_2 to c_2), and finally become a dominating dislocation cell pattern in R3 (Fig. 10a_1 to c_1).

Fig. 11 shows a typical exemplary ECCI investigation on the dislocation cell – annealing twin interaction in the specimen R4 with high magnification. The dislocation cells in the size of approximately 0.5–1 μm meet the existing annealing TBs and replacing the twinned

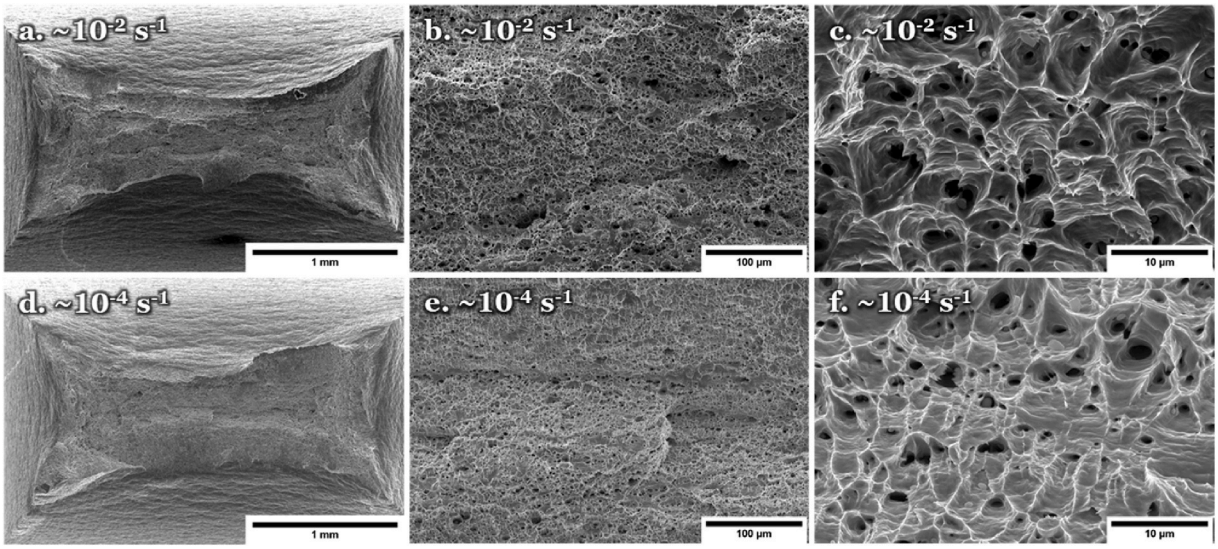

Fig. 3. Fractography of the Cu specimens monotonically tested at the a-c. Fastest (1×10^{-2}) and d-f. Slowest strain rate (1×10^{-4} s^{-1}). The fracture surface is displayed with three magnifications.

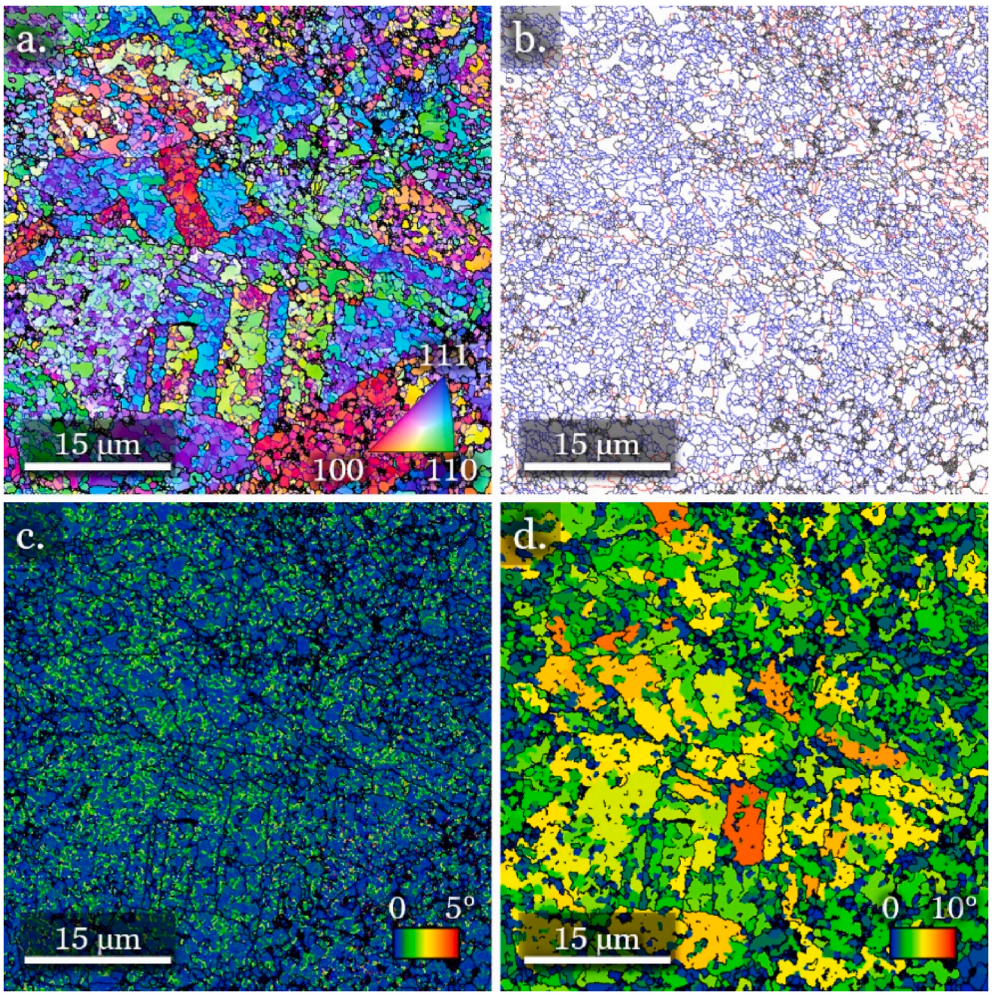

Fig. 4. Post-mortem analysis after monotonic testing ($\varepsilon > 10\%$) showing a. Orientation map with grain boundaries (black for HAGB and blue for LAGB); b. GB map (black HAGB + blue LAGB + red Σ3); c. KAM (sub grains) with HAGB and d. GOS with HAGB. (For interpretation of the references to color in this figure legend, the reader is referred to the Web version of this article.)

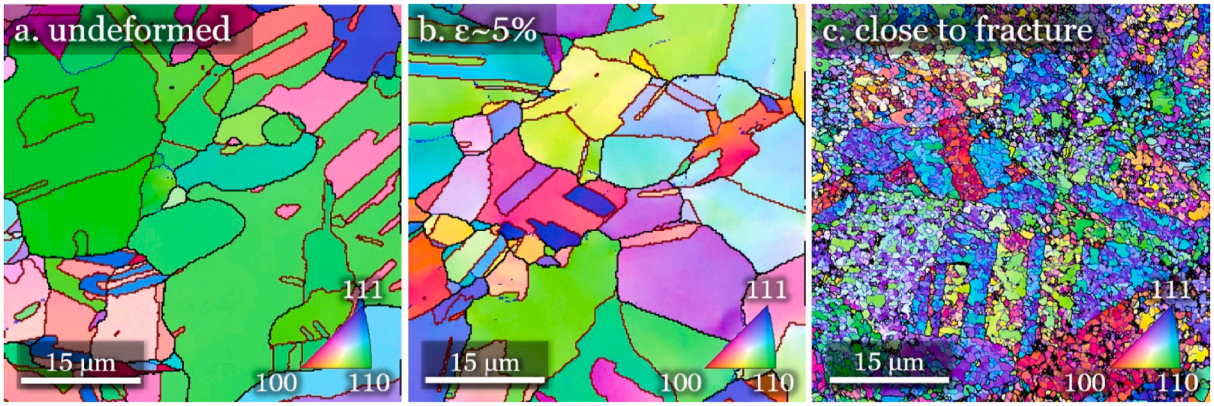

Fig. 5. EBSD grain orientation map of the microstructure after monotonic testing in a. Undeformed condition, b. After ~5% strain and c. Close to fracture.

microstructure with the polygonized dislocation cells. This is a typical detwinning process that creates a newly formed twin-free region [36]. Fig. 12 summarizes the TB fraction from EBSD analysis for all the investigated specimens in the current work. It is emphasized that the results in Fig. 12 are from at least four repeatable scans in random ROIs in the corresponding specimens and thus providing relatively good reliability. Clearly, the monotonic loading results in decreasing TB fraction with increasing strain level. Comparing the results from the cyclic loaded specimens, not only the increasing σ_m level, but also the increasing σ_a level results in a decreasing TB fraction in the deformed region. The R5 specimen has a similar TB fraction (~61.1%) as the initial non-tested microstructure (~60.4%), though plastic deformation can be detected in Fig. 10c_1 to c_3. This indicates that the relatively low σ_m and σ_a levels can generate dislocation activities, but not detwinning.

Table 3
Fraction of LAGBs HAGBs and Σ3 boundaries after various degrees of deformation.

Material	GB type	Fraction
Tensile test ε > 10%	LAGBs	0.374
	HAGBs	0.626
	Σ3	0.071
Static tensile ε ~5%	LAGBs	0.061
	HAGBs	0.939
	Σ3	0.572
Undeformed Cu	LAGBs	0.047
	HAGBs	0.953
	Σ3	0.604

While when the σ_a increases, the detwinning happens leading to the observed TB fraction decrease from ~60.4% in R5 to ~56% in R4. The increase in σ_m presents a more considerable detwinning effect that causes the TB fraction decrease from ~60.4% in R5 to ~17.2% in R3.

4. Discussion

4.1. Effect of test conditions: monotonic vs cyclic

As the current work is aimed at exploring the deformation and damage behavior of ETP Cu, especially regarding the creep-related phenomena, uniaxial tensile tests with different strain rates were performed. From the testing results, a ductile behavior was noticed for the studied material. The change in the applied strain rate (10^{-4} to 10^{-2} s^{-1}) did not cause much variation in the eventual failure resistance as observed through the monotonic tensile tests, but only the conventional shift in the strength (see Table 2). The ductile fracture of copper has already been extensively discussed in literature, e.g. in Ref. [37], and the strength increase with increasing strain rate (~9.8% and ~11.5% increase in the ultimate tensile strength when strain rate increases from 10^{-4} s^{-1} to 10^{-3} s^{-1} and 10^{-2} s^{-1}, respectively, see Table 2) is also unsurprising, e.g. in Ref. [38].

The stress-strain behavior shown in Fig. 2 a) reveals a typical ductile mechanical response, also confirmed by the relatively stable WHR is recorded in Fig. 2b for all three strain rates. In general, the ductility is largely governed by the WHR, which is in turn significantly influenced by the microstructural features that accommodate the deformation. From the microstructure analysis, the tensile loading elongates the grains along the loading direction at a relatively low strain level (Fig. 5b), and divides the deformed grains into subgrains at higher strain levels (Figs. 4 and 5c). In the beginning of plastic deformation, dislocation sources are activated by external loading, and dislocation multiplication becomes more and more significant. The dislocations intersecting the active slip planes (often referred to as forest dislocations) increase the resistance against the further dislocations motion and resulting in work hardening [39]. This is the classical theory explaining the general work-hardening behavior in the early stage of plastic deformation of metallic materials and has been well documented and generally accepted in textbooks [40].

In the current investigation, an interesting finding is the evolution of the annealing TB fraction. The detwinning process has been observed and reported in Cu specimens with a variety of microstructures [13,14,41,42], and is believed to affect the performance of structural parts [36]. TBs can act as conventional GBs in resisting dislocation motion due to its natural high-angle misorientation, and thus enhancing the flow stress during plastic deformation [43]. Results presented in Figs. 5 and 9b and Table 3 indicate that plastic deformation introduced dislocation multiplication and polygonization, which further create detwinning in the deformed areas and make the matrix twin-free. It is speculated that the observed detwinning procedure induces softening that competes with the dislocation multiplication leading to accumulation and storage (forest hardening). The equivalent contribution between the two

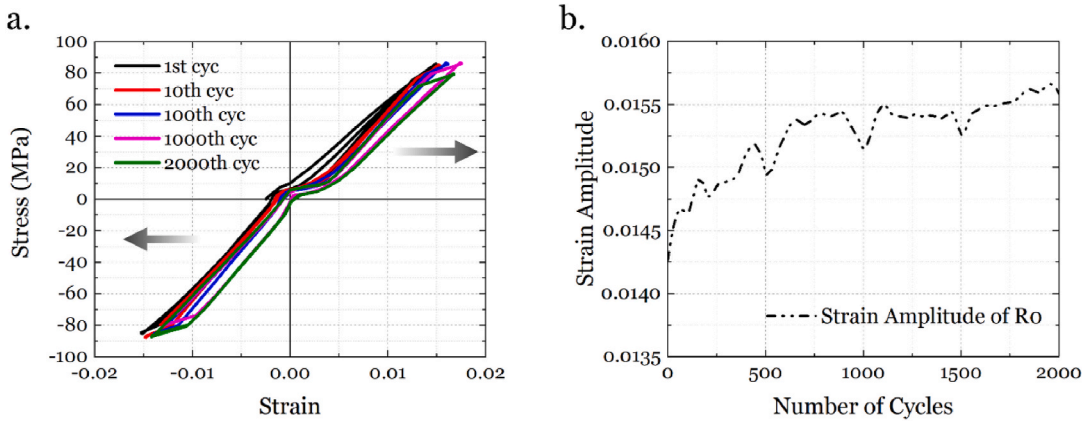

Fig. 6. The cyclic mechanical response from cyclic loading of R0: a. Typical hysteresis loop for specific cycles and b. The strain amplitude evolution with number of cycles.

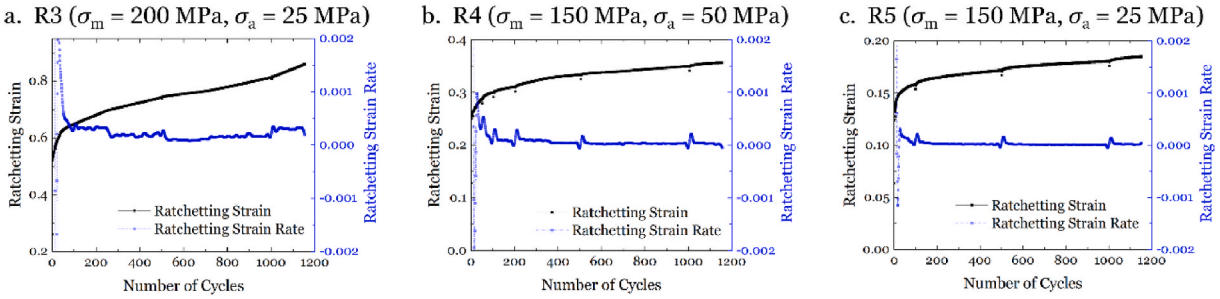

Fig. 7. The cyclic loading data for specimens a. R3 (σ_m = 200 MPa, σ_a = 25 MPa), b. R4 (σ_m = 150 MPa, σ_a = 50 MPa) and c. R5 (σ_m = 150 MPa, σ_a = 25 MPa).

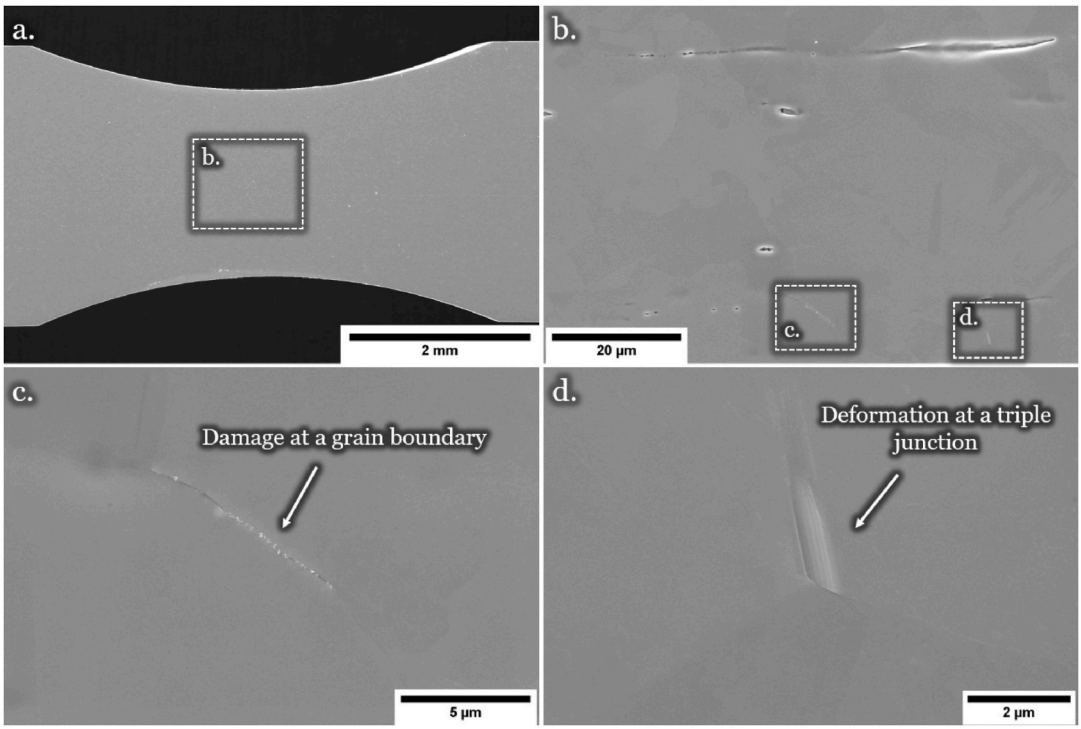

Fig. 8. SEM micrographs from *in-situ* cyclic tests of Cu, revealing the presence of grain boundary damage and deformation at triple point: a. Global morphology after 2000 cycles; b. Magnified region highlighted in a; c.&d. Magnified regions highlighted in b. The global loading direction is horizontal.

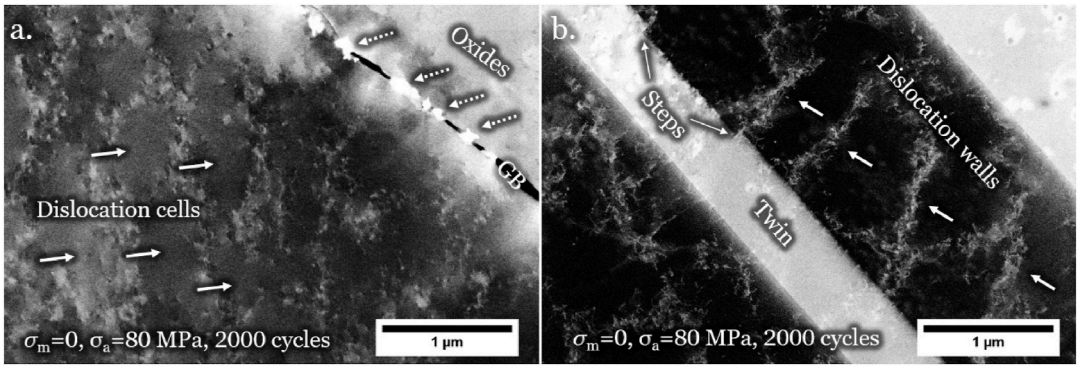

Fig. 9. ECC images from *in-situ* cyclic tests of Cu revealing a. The GB damage from Fig. 8c with the surrounding dislocation structure and b. The dislocation wall – TB interaction. The global loading direction is horizontal.

mechanisms results in a relatively stable WHR until a higher strain level is obtained, where the remaining TB fraction is not sufficient to be detwinned. As a result, dislocation activities become dominant in the deformation procedure (such as polygonization and subgrain formation). Hence, damages can initiate in the twin-free but dislocation-rich regions [28,44]. This can be evidenced by the EBSD analysis in Fig. 4 where a dominating subgrain structure with a rather limited TB fraction is noticed.

For the cyclic loading conditions, a softening behavior is noticed for all recorded cases (Figs. 6 and 7). For the simple case R0 ($\sigma_m = 0$ and $\sigma_a = 80$ MPa), the different stress-strain response from each load cycle can be explained by the cyclic slip irreversibility theory proposed by Mughrabi [45,46]. The dislocation motion during each loading cycle has an irreversible part that can result from annihilation of dislocations, loss of dislocations at surfaces, cross-slip of screw dislocations, etc., eventually affecting the global mechanical performance of the material. From the *in-situ* and post-mortem observations, surface damages are found to initiate at GBs or triple junctions (Figs. 8 and 9) due to accumulation of dislocations from multiple loading cycles. Furthermore, the dislocations form cells and walls inside the grains as well as interact with TBs and leave "empty" steps on the twin configuration (Fig. 9). The dislocation motion, dislocation – TB interaction together with the surface damages naturally introduce softening that can be responsible for the cyclic behavior of the R0 specimen. When considering the non-zero σ_m loading conditions for R3, R4 and R5, the tests can be described as cyclic ratchetting. If the three-stage ratchetting concept [47,48] is applied, the R4 and R5 specimens experienced only the primary and the secondary stage, where the tests stopped with a stable ratchetting strain rate versus number of cycles (Fig. 7b and c). The R3 specimen, featuring the highest σ_m, entered the tertiary zone of the cyclic ratchetting stages when the test terminated, as evidenced by a slightly increase in the ratchetting strain rate versus number of cycles (Fig. 7a).

It has been summarized in literature [48,49] that the primary stage in ratchetting (Stage I) is associated with the dislocation entanglement in grains, especially near GBs; the secondary ratchetting stage (Stage II) has dislocation veins, walls and incipient cells formation, and the

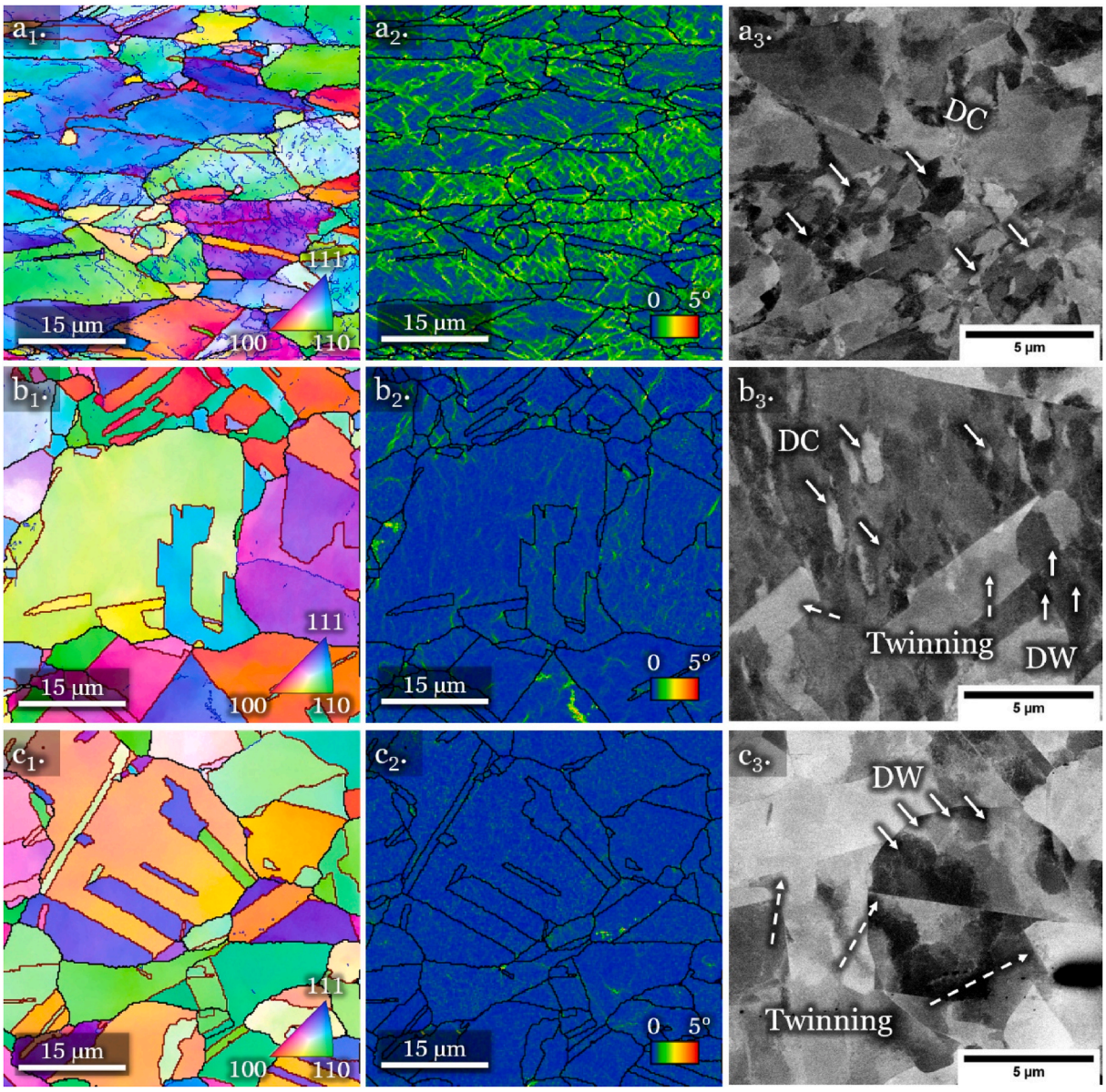

Fig. 10. Normal direction – orientation maps (1), KAM maps (2) and ECC images (3) of the cyclically loaded specimens $a_{1\text{-}3}$. R3 ($\sigma_m = 200$ MPa, $\sigma_a = 25$ MPa), $b_{1\text{-}3}$. R4 ($\sigma_m = 150$ MPa, $\sigma_a = 50$ MPa) and $c_{1\text{-}3}$. R5 ($\sigma_m = 150$ MPa, $\sigma_a = 25$ MPa). Note: the ROIs of the ECC images are not the same as that of EBSD analysis. (DC: dislocation cell; DW: dislocation wall).

tertiary stage (Stage III) has a more stable dislocation pattern configuration of dislocation cells more dominating than other less stable patterns. This can unambiguously explain the investigations in the current study. The R3 specimen, which touched the Stage III at the end of test, shows dominating dislocation cell structures in most of the grains in the ROI (Fig. 10a_2 and a_3), while the R4 and R5 specimen that were stopped in the Stage II comprise a dominating microstructure of early-stage dislocation cells and walls. It can be concluded that as σ_m and σ_a is increased, an early Stage III cyclic ratchetting may be activated together with the early formation of dislocation cell structures.

4.2. Evolution of twin boundaries with deformation

A noteworthy finding in the current work is the evolution of twin boundaries fractions during deformation of Cu. TB can simultaneously strengthen the material as well as act as barriers for fatigue crack propagation in Cu [44]. Understanding the behavior of TBs during loading will be beneficial to optimize the material performance in service. A general trend is that the TB fraction is decreasing with increasing deformation level. From the ECCI investigations in the current work, the change in the TB fraction is strongly associated with the detwinning behavior resulting from the dislocation – twin interaction both in monotonic deformation and in cyclic deformation. In the early-stage plastic deformation, the TBs can serve as a major source for dislocations in a non-regenerative manner [50]. Partial dislocations are continuously produced by consuming the existing annealing twins. Since detwinning plays a role of plasticity accommodation [41], this can probably be the reason behind the high ductility of pure Cu. As is evidenced from *in-situ* transmission electron microscopy, an Au [110] nanowire can have dislocation slip, deformation twinning and detwinning procedures depending on local stress fields owing to the interchange in Schmid factor between the leading and trailing partial dislocations [51]. The deformation mechanisms can have altered preferences during loading and unloading in one cycle and thus leaving permanent modification in the microstructure. In the case of cyclic loading of the investigated Cu specimens, complicated dislocation

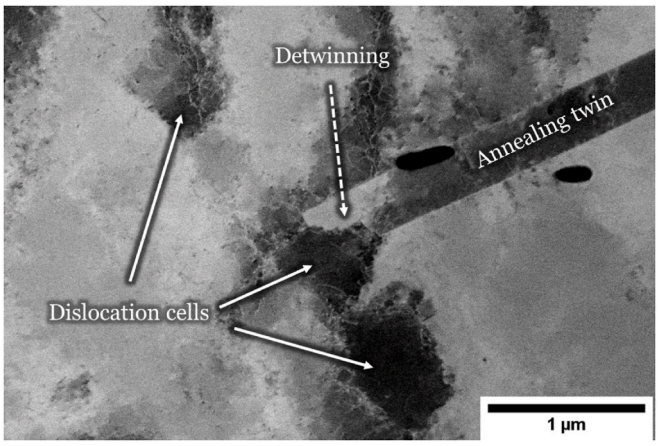

Fig. 11. ECC image of Cu specimen R4, revealing the detwinning procedure from dislocation cell – annealing twin interaction.

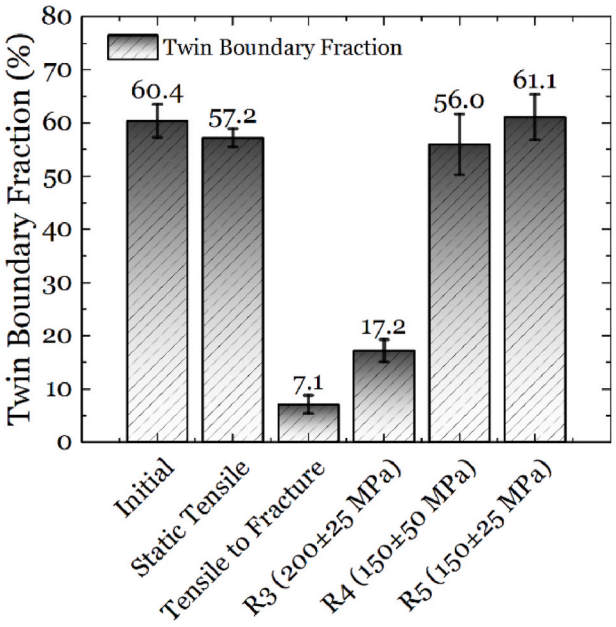

Fig. 12. TB fraction in the tested Cu specimens.

patterns are often generated such as walls and cells, and it seems that the dislocation cells are working more effectively in the detwinning process than dislocation walls. In the R0 specimen, the dislocation walls only created some steps on the TB (Fig. 9b). Similarly, the dislocation walls in R5 did not change the TB fraction drastically as can be read both from the microstructure analysis in Fig. 10 and the statistics in Fig. 12.

Comparing R3 to R5, the noteworthy detwinning happens in R4, where dislocation cells can be clearly observed, and becomes even more severe in R3 where the dislocation cells become a dominating deformation structure. It can be inferred that the detwinning happens when dislocations are forming cell structures. Considering the ratchetting stages, this process can be linked to the deformation mechanisms in the later Stage II and becomes more and more considerable as the ratchetting stage goes further. Since TBs are valuable sources of dislocation motion resistance and fatigue inhibitor, the loss of TB fraction during ratchetting fatigue can certainly influence the service life of the component. This suggests that the loading history will affect the fatigue life of the materials, i.e. instances of large plasticity load patterns detrimentally affects the material microstructure and potentially increases its susceptibility to fatigue damage.

A limitation in the present work comes from the number of tests, which so far covers a limited range of loading parameters. With the current results, a qualitative trend between the TB fraction evolution with respect to the stress levels can be presented, but finding a quantitative correlation between them is rather challenging at this stage. However, a test protocol can be proposed here for a future work by controlling different σ_m and σ_a values to cover a larger range with a given number of cycles. The same methodology of measuring TB fraction and dislocation patterns in the deformed specimen can be applied to explore the correlation between the mechanical performance and the microstructure evolution. In addition, cyclic testing at different strain rates is under planning and it is seen as a necessary further step in order to assess the impact of dynamic creep on the metallurgical evolution and creep-fatigue damage of the ETP-Cu.

5. Summary

In summary, the tensile and fatigue performance of an electrical grade Cu alloy (ETP Cu) was studied via small-scale *in-situ* mechanical testing. The microstructure evolution was intensively characterized by SEM-based techniques including EBSD and ECCI. The following conclusions are made:

- Upon monotonic tensile loading, the studied ETP Cu shows a ductile behavior. The strain rate in the range of 10^{-4} to 10^{-2} s^{-1} do not significantly change the behavior.
- Upon cyclic loading, the ETP Cu shows a softening trend both with and without mean stress.
- During tensile loading, dislocations prefer to entangle and polygonize to form wall and cell structures as strain increases. Significant subgrains formation can be seen in the fracture samples.
- Cyclic loading can also introduce dislocation walls and cells. At higher mean stress levels, dislocation evolution is faster that leads to later ratchetting stages.
- The twin boundary fraction in the microstructure has a significant dependence on the deformation status of the material. Lower twin boundary fraction indicates a less deformability. This may be used as an indicator for predicting the remaining life of the material in service.

Data availability

Some of the data required to reproduce these findings cannot be shared at this time as the data also forms part of an ongoing study.

CRediT authorship contribution statement

Di Wan: Data curation, Formal analysis, Investigation, Methodology, Writing – original draft. **Anette Brocks Hagen:** Project administration, Writing – review & editing. **Luigi Mario Viespoli:** Conceptualization, Writing – review & editing. **Audun Johanson:** Funding acquisition, Writing – review & editing. **Filippo Berto:** Writing – review & editing. **Antonio Alvaro:** Conceptualization, Project administration, Writing – review & editing.

Declaration of competing interest

The authors declare that they have no known competing financial interests or personal relationships that could have appeared to influence the work reported in this paper.

Acknowledgements

The present work was financed by Nexans Norway AS and the Research Council of Norway (IPN in ENERGIX Project number 296508) and performed within the project: New High Strength- High

Conductivity Aluminium Conductor Concept in Subsea Cables for Sustainable Energy Transport (NASCAR).

Appendix A. Supplementary data

Supplementary data to this article can be found online at https://doi.org/10.1016/j.msea.2022.142654.

References

[1] K. Grivas, A. Moraiti, G. Georgallis, G. Rinaldi, P.R. Thies, L. Johanning, Dynamic HV cables with AL conductors for floating offshore wind turbines: a cost and behavior comparative study, in: C. Guedes Soares (Ed.), The 4th International Conference on Renewable Energies Offshore (RENEW 2020), CRC Press, Lisbon, 2020.

[2] S. Khalilpourazary, M. Zadshakoyan, S.H. Hoseini, Ductile fracture analysis of annealed and ECAPed pure copper, Theor. Appl. Fract. Mech. 103 (2019), 102277.

[3] M. Zapara, N. Tutyshkin, W.H. Müller, R. Wille, A study of ductile damage and failure of pure copper – Part I: constitutive equations and experiments, Tech. Mech. 31 (2) (2011) 132–155.

[4] A. Sancho, M.J. Cox, T. Cartwright, P.A. Hooper, J.P. Dear, C.M. Davies, Effects of Strain Rate and Temperature on Ductile Damage of Metals, ASME 2018 Pressure Vessels and Piping Conference, ASME, Prague, 2018.

[5] W.D. Jenkins, T.G. Digges, Creep of annealed and cold-drawn high-purity copper, J. Res. Natl. Bur. Stand. 47 (4) (1951) 272–287.

[6] A. Perlega, Influence of Testing Frequency on the Fatigue Properties of Polycrystalline Copper, Institut für Festkörperphysik, TU Wien, 2015.

[7] L.M. Viespoli, A. Johanson, A. Alvaro, B. Nyhus, F. Berto, Strain controlled medium cycle fatigue of a notched Pb-Sn-Cd lead alloy, Eng. Fail. Anal. 104 (2019) 96–104.

[8] L.M. Viespoli, S. Bressan, T. Itoh, N. Hiyoshi, K.G. Prashanth, F. Berto, Creep and high temperature fatigue performance of as build selective laser melted Ti-based 6Al-4V titanium alloy, Eng. Fail. Anal. 111 (2020), 104477.

[9] M. Sobhaniasl, F. Petrini, M. Karimirad, F. Bontempi, Fatigue life assessment for power cables in floating offshore wind turbines, Energies 13 (12) (2020) 3096.

[10] A. Johanson, L.M. Viespol, A. Alvaro, F. Berto, Small- and Full-Scale Fatigue Testing of Lead Cable Sheathing, the 29th International Ocean and Polar Engineering Conference, International Society of Offshore and Polar Engineers, Honolulu, Hawaii, USA, 2019, p. 6.

[11] Y.H. Zhao, X.Z. Liao, Y.T. Zhu, Z. Horita, T.G. Langdon, Influence of stacking fault energy on nanostructure formation under high pressure torsion, Mater. Sci. Eng., A 410–411 (2005) 188–193.

[12] Y.-J. Li, K.-N. Tu, C. Chen, Tensile properties and thermal stability of unidirectionally <111>-Oriented nanotwinned and <110>-Oriented microtwinned copper, Materials 13 (5) (2020) 1211.

[13] L. Lu, Ultrahigh strength and high electrical conductivity in copper, Science 304 (5669) (2004) 422–426.

[14] L. Lu, X. Chen, X. Huang, K. Lu, Revealing the maximum strength in nanotwinned copper, Science 323 (5914) (2009) 607–610.

[15] R. Wang, H. Mughrabi, Fatigue of copper single crystals in vacuum and in air II: fatigue crack propagation, Mater. Sci. Eng. 65 (2) (1984) 235–243.

[16] R. Wang, H. Mughrabi, S. McGovern, M. Rapp, Fatigue of copper single crystals in vacuum and in air I: persistent slip bands and dislocation microstructures, Mater. Sci. Eng. 65 (2) (1984) 219–233.

[17] X.W. Li, Y.M. Hu, Z.G. Wang, Investigation of dislocation structure in a cyclically deformed copper single crystal using electron channeling contrast technique in SEM, Mater. Sci. Eng., A 248 (1–2) (1998) 299–303.

[18] Z.F. Zhang, Z.G. Wang, Effects of grain boundaries on cyclic deformation behavior of copper bicrystals and columnar crystals, Acta Mater. 46 (14) (1998) 5063–5072.

[19] J. Zhang, F. Xu, Y. Yan, T. Sun, Detwinning-induced reduction in ductility of twinned copper nanowires, Chin. Sci. Bull. 58 (6) (2013) 684–688.

[20] B. Wu, H. Fu, X. Zhou, L. Qian, J. Luo, J. Zhu, W.B. Lee, X.-S. Yang, Severe plastic deformation-produced gradient nanostructured copper with a strengthening-softening transition, Mater. Sci. Eng., A 819 (2021), 141495.

[21] N.M. Heckman, M.F. Berwind, C. Eberl, A.M. Hodge, Microstructural deformation in fatigued nanotwinned copper alloys, Acta Mater. 144 (2018) 138–144.

[22] G. Simons, C. Weippert, J. Dual, J. Villain, Size effects in tensile testing of thin cold rolled and annealed Cu foils, Mater. Sci. Eng., A 416 (1–2) (2006) 290–299.

[23] L. Llanes, C. Laird, The role of annealing twin boundaries in the cyclic deformation of f.c.c. materials, Mater. Sci. Eng., A 157 (1) (1992) 21–27.

[24] L. Llanes, C. Laird, Substructure evolution of copper polycrystals under different testing conditions: conventional strain control and ramp loading, Mater. Sci. Eng., A 161 (1) (1993) 1–12.

[25] L. Llanes, A.D. Rollett, C. Laird, J.L. Bassani, Effect of grain size and annealing texture on the cyclic response and the substructure evolution of polycrystalline copper, Acta Metall. Mater. 41 (9) (1993) 2667–2679.

[26] A.T. Winter, O.R. Pedersen, K.V. Rasmussen, Dislocation microstructures in fatigued copper polycrystals, Acta Metall. 29 (5) (1981) 735–748.

[27] J.C. Figueroa, S.P. Bhat, R. De La Veaux, S. Murzenski, C. Laird, The cyclic stress-strain response of copper at low strains—i. Constant amplitude testing, Acta Metall. 29 (10) (1981) 1667–1678.

[28] P. Zhang, Z.J. Zhang, L.L. Li, Z.F. Zhang, Twin boundary: stronger or weaker interface to resist fatigue cracking? Scripta Mater. 66 (11) (2012) 854–859.

[29] P. Zhang, Z.J. Zhang, L.L. Li, Z.F. Zhang, Corrigendum to "Twin boundary: stronger or weaker interface to resist fatigue cracking?", Scripta Mater. 67 (9) (2012) 795 [Scripta Mater 66 (2012) 854–859].

[30] S. Zaefferer, N.N. Elhami, Theory and application of electron channelling contrast imaging under controlled diffraction conditions, Acta Mater. 75 (2014) 20–50.

[31] A. Alvaro, D. Wan, V. Olden, A. Barnoush, Hydrogen enhanced fatigue crack growth rates in a ferritic Fe-3 wt%Si alloy and a X70 pipeline steel, Eng. Fract. Mech. 219 (2019).

[32] D. Wan, A. Alvaro, V. Olden, A. Barnoush, Hydrogen-enhanced fatigue crack growth behaviors in a ferritic Fe-3wt%Si steel studied by fractography and dislocation structure analysis, Int. J. Hydrogen Energy 44 (10) (2019) 5030–5042.

[33] D. Wan, A. Barnoush, Plasticity in cryogenic brittle fracture of ferritic steels: dislocation versus twinning, Mater. Sci. Eng., A 744 (2019) 335–339.

[34] I. Gutierrez-Urrutia, D. Raabe, Dislocation and twin substructure evolution during strain hardening of an Fe–22wt.% Mn–0.6wt.% C TWIP steel observed by electron channeling contrast imaging, Acta Mater. 59 (16) (2011) 6449–6462.

[35] M.S. Mirza, D.C. Barton, P. Church, J.L. Sturges, Ductile fracture of pure copper : an experimental and numerical study, J. Phys. IV 7 (C3) (1997). C3-891-C3-896.

[36] B.-G. Yoo, S.T. Boles, Y. Liu, X. Zhang, R. Schwaiger, C. Eberl, O. Kraft, Quantitative damage and detwinning analysis of nanotwinned copper foil under cyclic loading, Acta Mater. 81 (2014) 184–193.

[37] J.L. Wang, M.W. Fu, S.Q. Shi, Influences of size effect and stress condition on ductile fracture behavior in micro-scaled plastic deformation, Mater. Des. 131 (2017) 69–80.

[38] J.L. Jordan, C.R. Siviour, G. Sunny, C. Bramlette, J.E. Spowart, Strain rate-dependant mechanical properties of OFHC copper, J. Mater. Sci. 48 (20) (2013) 7134–7141.

[39] Z.S. Basinski, S.J. Basinski, Dislocation distributions in deformed copper single crystals, Philos. Mag. 9 (97) (1964) 51–80.

[40] G. Gottstein, Physical Foundations of Materials Science, Springer-Verlag Berlin Heidelberg, New York, 2004.

[41] M.J. Szczerba, S. Kopacz, M.S. Szczerba, Experimental studies on detwinning of face-centered cubic deformation twins, Acta Mater. 104 (2016) 52–61.

[42] J. Gu, L. Zhang, S. Ni, M. Song, Formation of large scaled zero-strain deformation twins in coarse-grained copper, Scripta Mater. 125 (2016) 49–53.

[43] P. Zhang, Q.Q. Duan, S.X. Li, Z.F. Zhang, Cyclic deformation and fatigue cracking behaviour of polycrystalline Cu, Cu–10 wt% Zn and Cu–32 wt% Zn, Philos. Mag. 88 (16) (2008) 2487–2503.

[44] Z. Zhang, L. Li, Z. Zhang, P. Zhang, Twin boundary: controllable interface to fatigue cracking, J. Mater. Sci. Technol. 33 (7) (2017) 603–606.

[45] H. Mughrabi, Cyclic slip irreversibilities and the evolution of fatigue damage, Metall. Mater. Trans. B 40 (4) (2009) 431–453.

[46] H. Mughrabi, Cyclic slip irreversibility and fatigue life: a microstructure-based analysis, Acta Mater. 61 (4) (2013) 1197–1203.

[47] S.K. Paul, A critical review of experimental aspects in ratcheting fatigue: microstructure to specimen to component, J. Mater. Res. Technol. 8 (5) (2019) 4894–4914.

[48] G. Kang, Ratchetting: recent progresses in phenomenon observation, constitutive modeling and application, Int. J. Fatig. 30 (8) (2008) 1448–1472.

[49] G. Kang, Q. Kan, Cyclic Plasticity of Engineering Materials, 2017.

[50] S. Ifergane, Z. Barkay, O. Beeri, N. Eliaz, Study of fracture evolution in copper sheets by in situ tensile test and EBSD analysis, J. Mater. Sci. 45 (23) (2010) 6345–6352.

[51] S. Lee, J. Im, Y. Yoo, E. Bitzek, D. Kiener, G. Richter, B. Kim, S.H. Oh, Reversible cyclic deformation mechanism of gold nanowires by twinning-detwinning transition evidenced from in situ TEM, Nat. Commun. 5 (1) (2014) 3033.